J. Mech. Phys. Solids 204 (2025) 106282

Contents lists available at ScienceDirect

Journal of the Mechanics and Physics of Solids

journal homepage: www.elsevier.com/locate/jmps

Modeling semi-flexible biopolymer networks with geometrically exact, non-linear isogeometric beams

Matthew J. Lohr[1], Soham Mane[1], Sotirios Kakaletsis, Grace N. Bechtel, Jan N. Fuhg, Berkin Dortdivanlioglu, Rui Huang, Manuel K. Rausch *

The University of Texas at Austin, United States of America

ARTICLE INFO

Keywords:
Elastin
Collagen
Fibrin
Bending strip
Planar biaxial extension

ABSTRACT

Biopolymers are an important class of materials that comprise many biological tissues. Their semi-flexible nature sets them apart from most synthetic polymers. Thus, the development of material-specific models is an important step toward understanding their structure-function relationship. This, in turn, will enable us to understand biological tissues such as heart valves, arteries, and skin. Here we propose and test the use of geometrically-exact, nonlinear isogeometric beams and beam assemblies to model semi-flexible polymer networks. Beyond establishing and validating this modeling framework, we demonstrate its potential by exploring the deformations of individual fibers and of 3D semi-flexible biopolymer networks. We do so in networks of straight and undulated fibers and find that fiber geometry significantly alters the networks' macro-mechanics. Additionally, we find that fibers undergo a well-preserved sequence of loading modes. Specifically, fibers first reorient and bend and are then uniaxially stretched. We further showcase our framework by successfully comparing a fibrin pure shear experiment against our model predictions. We believe that our modeling framework will be useful in continuing the investigation of the structure-function relationships of semi-flexible biopolymer networks and will thus provide insight into the mechanics of biological tissues.

1. Introduction

Biopolymers are the building blocks of life (Matange et al., 2025). They form the structural backbone of our soft tissues (Picu, 2011), give cells their shape (Riedel et al., 2025), and enable many physiological functions (Tsingos et al., 2023; Tang, 2020). They are also often implicated in severe diseases, including cancer (Chacko et al., 2023; Pearce et al., 2023). Thus, understanding the mechanical behavior of biopolymers is a critical step toward understanding our bodies' functions and dysfunction. As the name suggests, biopolymers are naturally occurring materials that form by adding monomeric units (Yadav et al., 2015). Examples of biopolymers are DNA, a polynucleotide, glucose, a polysaccharide, and fibrin/collagen, representatives of polypeptides (Runnels et al., 2018). Understanding the mechanical behavior of collagen, fibrin, and elastin is particularly important to biomechanics, as they form the structural elements of many types of tissue in our bodies, see Fig. 1 (Ferruzzi et al., 2013; Ling et al., 2019; Wang et al., 2021). For example, collagen is the primary structural protein in skin (Meador et al., 2020b), ligament (Bastas et al., 2025), cartilage (Chawla et al., 2024), tendon (Korcari et al., 2023), heart valves (Meador et al., 2020a), and other types of soft tissue (Kakaletsis et al., 2021; Middendorf et al., 2021). Elastin is the key to the stretchability of many of these tissues (Tarakanova

* Corresponding author.
E-mail address: manuel.rausch@utexas.edu (M.K. Rausch).
[1] Shared first authorship.

https://doi.org/10.1016/j.jmps.2025.106282
Received 17 March 2025; Received in revised form 22 May 2025; Accepted 10 July 2025
Available online 21 July 2025

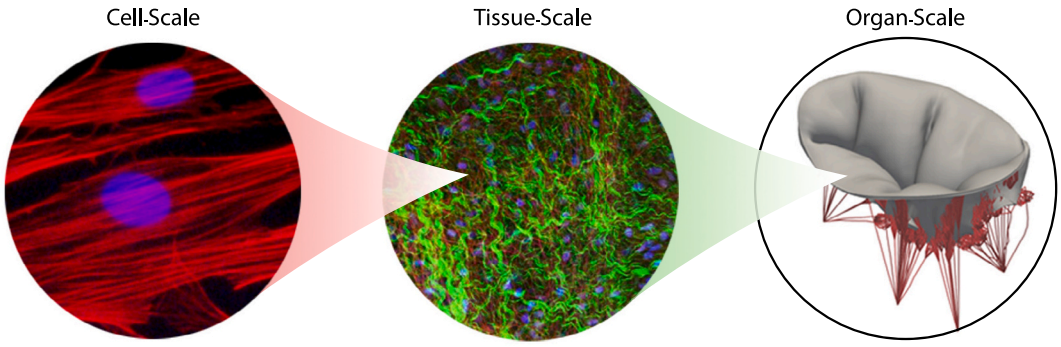

Fig. 1. Semi-flexible biopolymer networks comprise many soft tissues. Shown are an actin cytoskeleton on the cellular scale, which has been adapted from Hashimoto et al. (2017), and collagen (green)/elastin (red) on the tissue scale of a tricuspid valve leaflet (Meador et al., 2022; Haese et al., 2025). The organ scale image is that of a human tricuspid valve in which the leaflets are shown in gray and the chordae tendineae are shown in red (Mathur et al., 2022).

et al., 2018), and fibrin forms the backbone of blood clots that play a critical role in our cardiovascular system, preventing bleeding after vascular injury (Lohr et al., 2022, 2025). Like synthetic polymers, collagen, fibrin, and elastin form fibers that assemble into fibrous networks that can be physically entangled, weakly bonded, or covalently bonded via cross-links (Amuasi et al., 2012; Jansen et al., 2018). However, in contrast to most synthetic polymers, these structural biopolymers are semi-flexible (Broedersz and MacKintosh, 2014). That is, they have significant bending stiffness, and their mechanics are governed primarily by their strain energy rather than entropy. Due to the complex and non-affine mechanics of such networks, numerical models are important to both our understanding of their structure-function relationship and to predicting their behavior in response to loading (Jansen et al., 2018). The goal of this work is to develop a framework that lends itself to realistic representations of this important class of materials.

There has been substantial previous work toward computational modeling of discrete fiber networks (Negi and Picu, 2019; Picu, 2011). Previous approaches have differed in four key aspects: (i) their network representation, i.e., how they modeled the complex, natural architectures of these networks, including fiber geometry, characteristic network length, fiber connectivity, and dimension (Carleton et al., 2015; Islam and Picu, 2018; Picu et al., 2020). Most of the previous work employs random processes (e.g., Voronoi tessellation) to create representative networks (Kallel and Joulain, 2022; Eichinger et al., 2021). Alternatively, some studies derived network topologies from SEM or fluorescence microscopy images (Shkarin et al., 2019); (ii) their fiber constitutive behavior. Previous approaches have included phenomenological models akin to linear or non-linear elastic springs (Arzash et al., 2020). Hyperelastic material models have also been employed (Hall et al., 2016); (iii) their fiber-level kinematic assumptions. Although many previous studies have approximated fibers as tension-only elements (Rodney et al., 2005), i.e., springs without bending or torsional stiffness, others have employed more complex theories such as Euler–Bernoulli (Zakharov et al., 2024) or Timoshenko beam theory (Merson and Picu, 2020; Timoshenko, 1953); finally, (iv) their solution strategy. Performance-oriented approaches used non-linear truss solvers, such as those of Stylianopoulos et al. and Leng et al. who used a volume averaging technique to couple their network problem to the integration point level of a finite element problem (Stylianopoulos and Barocas, 2007; Leng et al., 2021). On the other hand, most of the other approaches used the standard C^0-continuous finite element method (Dey et al., 2024).

In the current work, we build on these prior efforts. However, in contrast to all prior work, we use isogeometric analysis to represent the individual fibers. We do so to take advantage of the inherent ability of isogeometric analysis to exactly represent complex curved geometries and its numerical ability to represent C^1-continuous higher-order beam formulations (Hughes et al., 2005). Furthermore, we use large deformation-compatible material laws, beam kinematics that include membrane, bending, and torsion effects, and rely on Voronoi tessellation to build 3D network topologies (Bauer et al., 2016). Once implemented, we verify our framework by means of single-fiber examples and showcase its abilities with fully 3D fiber networks. In these networks, we explore the structure-function relationship of straight fiber and undulated fiber networks under planar biaxial extension. Additionally, we validate our framework against original pure shear fibrin gel experiments.

2. Methods

2.1. Geometrically exact, non-linear isogeometric spatial beam

Toward building 3D semi-flexible biopolymer networks, we first model individual fibers as geometrically exact, non-linear isogeometric beams, see Fig. 2. Here, we note that, throughout this work, we normalized all the quantities of interest. In doing this, we did not specifically calibrate our networks to represent a particular type of biopolymer. We define the constitutive behavior of these fibers as linearly elastic with Young's modulus E and Poisson ratio ν. To this end, we follow exactly the formulation of Bauer et al. (2016). According to the assumptions of the Euler–Bernoulli beam theory, the cross section of the fibers remains orthogonal to the center line, and the cross-sectional area of the fibers does not change. The beam is thus represented only by a center line and

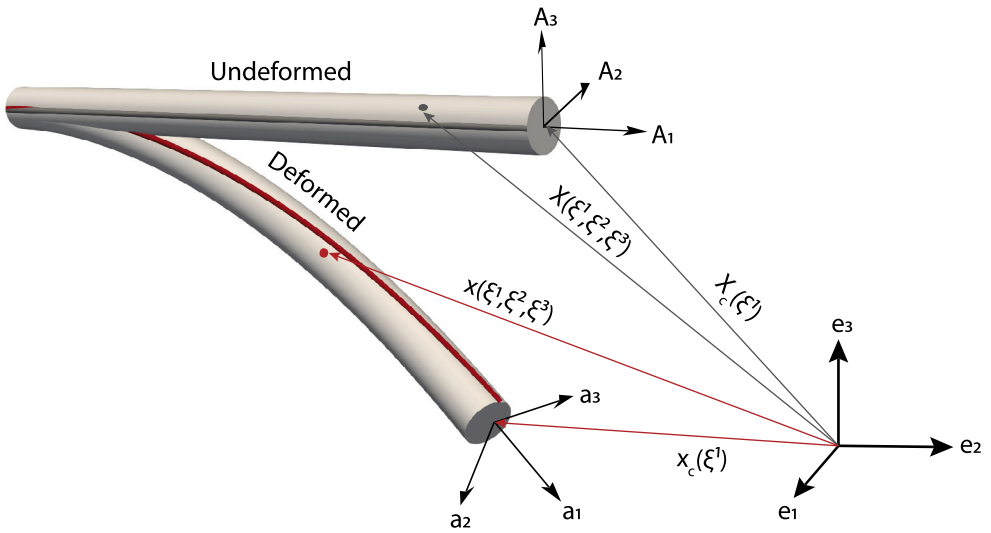

Fig. 2. Beam kinematics to approximate the deformation of slender fibers. The deforming beam is described via the motion of its center line and a moving trihedral whose bases are of unit length and orthogonal to the center line. Note, the beam cross section does not warp as the beam deforms.

a moving trihedral. Please note that, in contrast to the traditional bending-only treatment of Euler–Bernoulli beams, we do include both membrane and torsion energies in this present formulation. Based on these kinematic assumptions, the beam formulation reduces to three displacement degrees of freedom and one rotational degree of freedom. The latter measures the relative rotation of the fiber about the center line. This assumption is appropriate for slender fibers, where the fiber's length is significantly larger than the fiber's cross-sectional dimension (i.e., radius). Based on these geometric assumptions, the position vectors for each point on the beam follow as

$$\mathbf{X}\left(\xi^1,\xi^2,\xi^3\right)=\mathbf{X}_c\left(\xi^1\right)+\xi^2\mathbf{A}_2\left(\xi^1\right)+\xi^3\mathbf{A}_3\left(\xi^1\right), \tag{1}$$

$$\mathbf{x}\left(\xi^1,\xi^2,\xi^3\right)=\mathbf{x}_c\left(\xi^1\right)+\xi^2\mathbf{a}_2\left(\xi^1\right)+\xi^3\mathbf{a}_3\left(\xi^1\right), \tag{2}$$

where $\mathbf{X_c}$ and $\mathbf{x_c}$ are position vectors of the center line in the reference and current configurations, respectively, ξ^i are the contravariant coordinates and A_i as well as a_i are base vectors aligned with the moving trihedral in the reference and current configurations, respectively. See Fig. 2 for an illustration of these kinematic quantities. For technical details on the alignment of the moving trihedral in the reference and current configurations, we refer the reader to the original work by Bauer et al. (2016)

The isogeometric analysis method, just like the standard non-linear finite element method, derives the solution to the balance of linear momentum through the principle of virtual work (Tepole et al., 2015; Hughes et al., 2005). In turn, the principle of virtual work gives rise to the weak form of the problem that may then be discretized, linearized, and iteratively solved (e.g., via Newton–Raphson methods). Although linearization and solution techniques are equivalent to the finite element method, spatial discretization of the problem domain follows from the use of Non-Uniform Rational B-Splines (NURBS) shape functions (Piegl and Tiller, 1996). Specifically, we interpolate the spatial coordinates of the beam center line, $\mathbf{x}_c$, via

$$\mathbf{x}_c=\sum_i N_{i,p}\hat{\mathbf{x}}^i, \tag{3}$$

where $\hat{\mathbf{x}}^i$ are position vectors of the control points and $N_{i,p}$ are NURBS shape function of order p.

For complete details on structural mechanics and element formulations, we refer the reader to previous work (Bauer et al., 2016, 2020). However, we briefly introduce NURBS in the next section, as they are central to our approach. We also note that we did not implement direct fiber-to-fiber contact, and junctions are predefined with a bending strip technique, see below.

2.2. Nonuniform rational basis spline - NURBS

In contrast to the standard finite element formulation where geometries are discretized via "elements", geometries in the isogeometric framework are discretized via B-spline-based patches. Each B-spline patch is partitioned into elements by so-called "knots". In turn, knots are organized in knot vectors, a non-decreasing set of coordinates in the parameter space, written as $\Xi=\left\{\xi_1,\xi_2,\ldots,\xi_{n+p+1}\right\}$, where $\xi_i\subset R$ is the ith knot, i is the knot index, $i=1,2,\ldots,n+p+1$, p is the polynomial order, and n is the

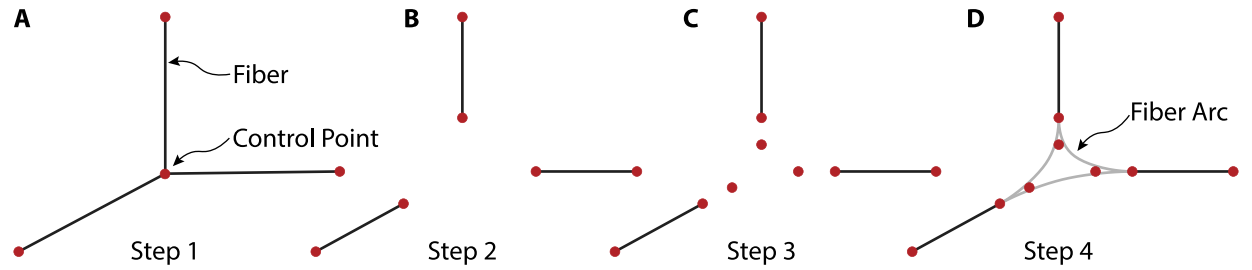

Fig. 3. Bending strip technique. (A) The fibers are connected at a common node in the original network. (B) The fibers are trimmed. (C) New control points are inserted to generate circular arcs. (D) These fiber arcs connect the new fiber endpoints. Bending strips connect the ends of the fiber arcs to the ends of the fibers.

number of basis functions used to construct the B-spline curve. The B-spline basis functions, $Q_{i,p}(\xi)$, are then defined recursively via the Cox-de Boor recursion formula starting with piecewise constants ($p = 0$) (Cox, 1971; De Boor, 1972):

$$Q_{i,0}(\xi) = \begin{cases} 1 \text{ if } \xi_i \le \xi < \xi_{i+1}, \\ 0 \text{ otherwise.} \end{cases} \tag{4}$$

For $p = 1, 2, 3, \ldots$, they are defined by

$$Q_{i,p}(\xi) = \frac{\xi - \xi_i}{\xi_{i+p} - \xi_i} Q_{i,p-1}(\xi) + \frac{\xi_{i+p+1} - \xi}{\xi_{i+p+1} - \xi_{i+1}} Q_{i+1,p-1}(\xi). \tag{5}$$

NURBS, in turn, are obtained through the projective transformation of B-splines as per

$$N_i^p(\xi) = \frac{Q_{i,p}(\xi) w_i}{W(\xi)}. \tag{6}$$

Here, $W(\xi)$ is a weighting function calculated by

$$W(\xi) = \sum_{i=1}^{n} Q_{i,p}(\xi) w_i \,, \tag{7}$$

where w_i is the weight assigned to control point i. Because NURBS are rational functions, they are inherently capable of capturing the spatially curved nature of individual fibers to any desired degree of curvature. This property makes NURBS an ideal choice for modeling semi-flexible biopolymers. Further details on B-splines and NURBS can be found in the work by Hughes et al. (2005) and Piegl and Tiller (1996).

2.3. Beam bending strip formulation

In order to transition from single fibers to fiber networks within the isogeometric formulation, it is necessary to devise a strategy to link the discretized patches. The above Euler–Bernoulli beam formulation demands C^1-continuity across the entire beam domain. However, only C^0-continuity is ensured at the boundaries of NURBS patches. Thus, multi-patch beams require special treatment. Although Bauer et al. have used multi-point constraints to ensure sufficient continuity across patch boundaries (Bauer et al., 2020), we instead chose to adopt a technique popularized for shell formulations. Specifically, we introduce the so-called "bending strips" (Kiendl et al., 2010). In its essence, the bending strip technique is a penalty method in which we penalize the change in angle of the connected components without adding any membrane stiffness to the system. Thus, the strip facilitates the transfer of bending moments between the connected components. This method was previously extended from shells to the isogeometric cable formulation by Raknes et al. (2013). We adopted this technique in our current work to combine multiple beam patches, allowing us to attach individual beams and construct entire beam networks. Because the bending strip technique is natively limited to combining two patches at a time, but semi-flexible biopolymer networks may have both "Y"- and "X"-junctions, at which three or four fibers may connect, we devised an appropriate implementation strategy shown in Fig. 3: (i) We trim the fibers at the junctions to reduce the fiber length by $\approx 2\%$ of their original length. (ii) We create three circular arcs for Y-junctions or four circular arcs for X-junctions that are tangent to the fiber ends. (iii) We discretize each fiber arc with two NURBS elements of order two. (iv) We connect the fiber arcs and fiber ends by bending strips.

2.4. Random network generation

Our strategy of combining isogeometric Euler–Bernoulli beams with the bending strip technique is amiable to any network topology. In this current work, we created 3D networks using a Voronoi-based approach. Specifically, we generated Voronoi networks from random seeds and then enforced realistic connectivity numbers for semi-flexible biopolymers (Kakaletsis et al., 2023). We accomplished this by iteratively removing fibers with local connectivity numbers of $z >= 4$ until we reached our target value. Here, we chose $z = 3.4$, which falls in the range of typical values for fibrin networks ($z \in [3, 4]$) (Garyfallogiannis et al., 2023).

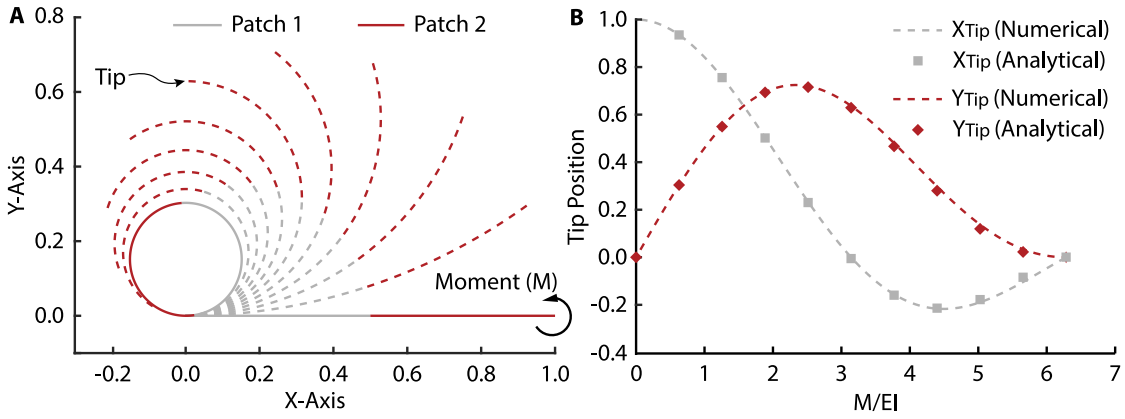

Fig. 4. The Mainspring verification problem. In this problem, we apply a point moment to the end of a cantilevered beam. (A) The solid lines represent the initial and final deformed states of the fiber, while dashed lines show the fiber's states at different points throughout the loading. We used two patches with NURBS of order six and 10 elements each. (B) Our results compare well to those of Bauer et al. (2016).

2.5. Fibrin gel fabrication and mechanical testing

We prepared fibrin gels by reconstituting bovine fibrinogen (Thermo Fisher Scientific, Waltham, MA, USA; Catalog No. J63276, Lot No. U06G021) in 1× phosphate-buffered saline (PBS, pH 7.4) to a final concentration of 10 mg/mL. Based on protein density, this concentration corresponds to a fibrin network volume fraction of approximately 0.75%. We then added 10% (w/v) $CaCl_2$ and thrombin (MilliporeSigma, Burlington, MA, USA; Catalog No. 605195, Lot No. 4238521) to final concentrations of 5 mM and 2.5 U/mL, respectively. Following gentle mixing, we cast the solution into 3D-printed molds designed to interface with our mechanical testing apparatus (Instron, Norwood, MA, USA), yielding samples with dimensions of 40 × 10 × 3 mm. Molds were lined with Velcro to ensure a secure attachment between the gel and fixture, as in our prior mechanical testing of soft materials (Sugerman et al., 2021, 2024; Bechtel et al., 2025a,b). We incubated samples at 37 °C for 60 min prior to testing. We then mounted samples onto the Instron and extended them to failure at a strain rate of 0.2 mm/s. Throughout testing, we measured force with a 10 N load cell (± 0.02 N accuracy) and recorded the displacement.

3. Results

3.1. Validation problems

We performed three benchmark problems to (i) confirm the correct implementation of the isogeometric Euler–Bernoulli beam formulation, and (ii) verify that the bending strip technique yields accurate results. To this end, we chose the following standard problems: the Mainspring Problem, the Shallow Arch Problem, and the 45-Degree Bend Under Bending and Torsion.

Mainspring Benchmark. This is an in-plane problem where we apply a point moment to the free end of a cantilevered beam. The beam bends into a full circle when loaded with a point moment of $M = 2\pi EI/L$, where E is Young's modulus, I is the moment of inertia, and L is the length of the beam. We used two patches with NURBS of order six and 10 elements each. Fig. 4A shows a comparison between our numerical results and the analytical solution to this problem (Bauer et al., 2016). Our results compare well to the analytical solution, see Fig. 4B.

Shallow Arch Snap-Through Benchmark. A shallow arch is supported at both ends and is loaded with a point load at its apex, see Fig. 5A. As the load is applied, the arch deforms and snaps through at a critical load. We used two patches with NURBS of order six and 16 elements each, see Fig. 5. Our results compare well to those of a previous work (Lo, 1992).

45-Degree Bend Under Combined Bending and Torsion Benchmark. In this problem, a 45-degree circular arc lies in the bottom plane. The arc is clamped at one end, while the other end is loaded with an out-of-plane point force. The force bends and twists the circular arc into a 3D space curve. We used two patches with NURBS of order six and 16 elements each. The resulting end tip displacement of $x = -13.74, y = -23.55, z = 53.56$ at the end of the loading compares well with literature values that range between $x \in [-14.05, -13.4]$, $y \in [-24.25, -23.42]$, $z \in [53.3, 54.55]$ (Marino, 2017), see Fig. 6.

3.2. Single fiber simulations

Planar Undulated Fiber. Before applying our approach to semi-flexible biopolymer networks, we set out to investigate the mechanical behavior of individual fibers with an end-to-end length of $L = 1$, a cross sectional radius of 10^{-3}, a Young's Modulus of $E = 10^6$, and a Poisson ratio of $\nu = 0.2$. Furthermore, we applied an undulation to the fiber in the X–Y plane with an amplitude of 0.1. We discretized the fiber with a single patch of order five and 64 elements. We applied a point load to the right end of the

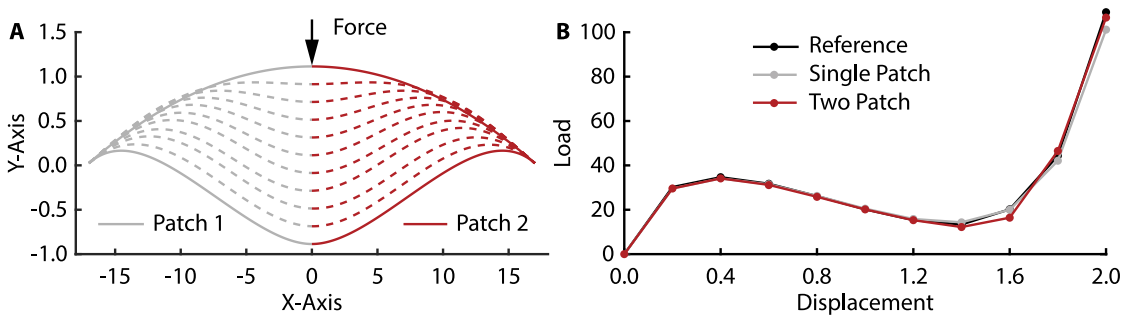

Fig. 5. The Shallow Arch verification problem. (A) We apply a point load to the arch's apex. We used two patches with NURBS of order six and 16 elements each. (B) The load–displacement curve shows the snap-through characteristic of the arch as it is displaced by the point load. Our results compare well to those of a previous work (Lo, 1992).

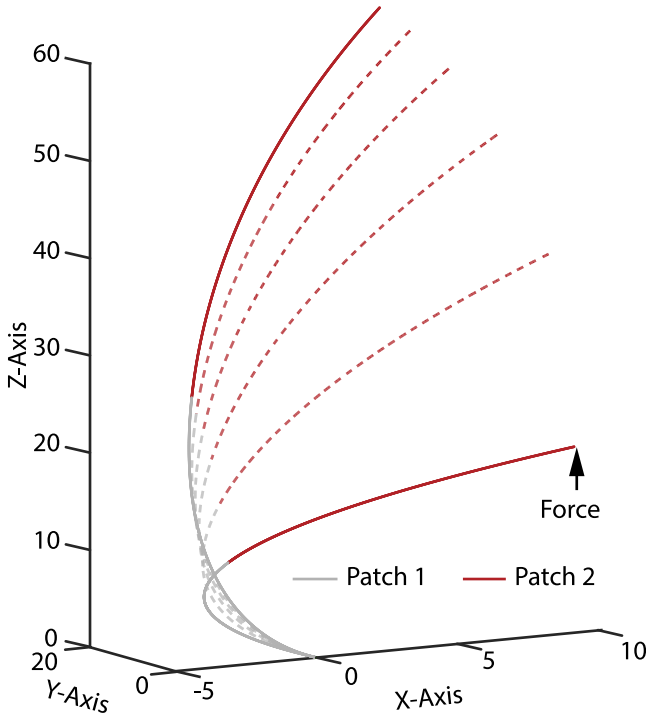

Fig. 6. The Combined Bending and Torsion problem. A 3D space curve made of two NURBS patches connected through a bending strip is bent out of plane by an end-point load. Both patches are of order six and are discretized with 16 elements each. Our results compare well to those in the literature (Marino, 2017).

fiber in the x-direction, and we pinned the other end of the fiber. Fig. 7A illustrates the normalized load–displacement curve. This curve demonstrates that the undulated fiber response is non-linear despite the linear constitutive behavior of the fiber material. Fig. 7B reveals that the load–displacement non-linearity arises from a transition in the strain energies during loading. While the load–displacement behavior is governed by bending energy due to fiber straightening under small strains, it is governed by membrane energy at large strains. Thus, the apparent non-linearity in the fiber response stems from the fiber geometry alone.

Non-planar Undulated Fiber. Similar to our testing of a planar undulated fiber, we also investigated the mechanics of a non-planar undulated fiber. The fiber had the same material and geometric properties as the fiber above. However, in addition to the undulation in the X–Y plane, we applied the same undulation in the X–Z plane. Figs. 8A–B show the load–displacement curve and energy fractions, respectively. Similarly to the planar fiber, the load–displacement behavior is non-linear despite the material's linear constitutive behavior. In contrast to the planar undulated fiber, the total energy stored in the fiber is comprised of membrane, bending and torsion energy. However, the torsion energy contributes only marginally to the total fiber energy under large strains, see Fig. 8B. Hence, qualitatively, the non-planar undulated fiber behaves very similarly to the planar undulated fiber. However, quantitatively, the "stiffening point", i.e., the point where the fiber response deviates markedly from being linear, shifts

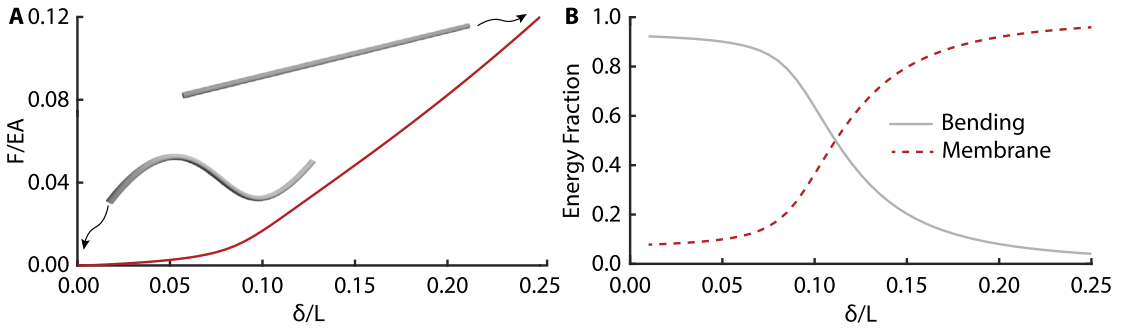

Fig. 7. Mechanics of a planar undulated fiber subject to loading. (A) Non-linear load–displacement behavior of the fiber, where the force F was normalized by the axial rigidity EA, and the displacement δ was normalized by the projected length L of the fiber. (B) Energy fractions in the fiber that transition from being bending dominated to membrane dominated.

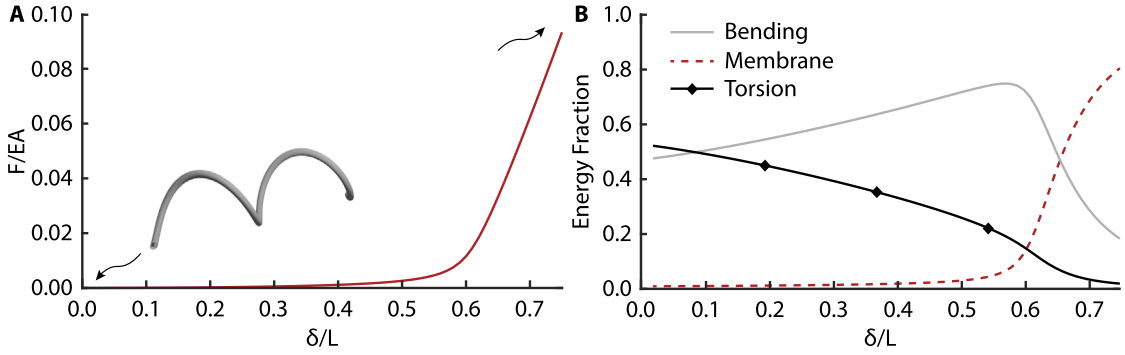

Fig. 8. Mechanics of a non-planar undulated fiber subject to loading. (A) Non-linear load–displacement behavior of the fiber. Again, the applied force F was normalized by the axial rigidity EA, and the displacement δ was normalized by the fiber length, L. (B) Energy fractions in the fiber that transition from being bending and torsion dominated to membrane dominated.

to a significantly higher strain compared to the planar fiber. The reason for this shift is, at least in part, due to the increased arc length of the non-planar fiber resulting from the additional undulation into the third dimension.

3.3. 3D network simulations

We demonstrated our framework through two examples. First, we simulated 300-fiber networks under biaxial tension. Because many, if not most, semi-flexible polymer networks are undulated, we compared the mechanics of straight and undulated networks in this example. For undulated networks, we applied sinusoidal undulations to each fiber in the local A_2 and A_3 directions of each fiber. The amplitude of these undulations was 0.025. Second, we demonstrated that our networks can match the experimental data collected from real fibrin gels. To this end, we fit a 380-fiber network's response against the force–displacement data of a fibrin gel under pure shear loading.

In our first virtual network experiment, we exposed three mini networks made of straight and undulated fibers to planar biaxial extension, see Fig. 9A. That is, we displaced the fiber nodes within the $x = 1$ and $y = 1$ faces, while holding those fiber nodes within the $x = 0$ and $y = 0$ faces fixed. The fiber nodes within the $z = 0$ and $z = 1$ faces were left traction free. The original topology of the straight and undulated networks was identical, allowing for direct comparisons between the two types of networks. In Fig. 9, we see responses of both network types. The straight fiber networks are primarily governed by bending and torsion deformations until a transition point at 5% strain at which the membrane energy begins to dominate, see Fig. 9B on the left. Similarly, in the undulated network, bending and torsion dominate until a transition point at 4% strain at which membrane energy, again, begins to dominate, see Fig. 9B on the right. Please note that in calculating the energy fractions of the networks, we excluded the energies in the bending strips and arcs connecting fibers. Fig. 9C shows the resulting mean stress–strain behavior of both types of networks as well as their ranges. Here, as in the single-fiber cases, we see non-linearity arising. Again, this non-linearity does not stem from the constitutive behavior of the fibers, but rather from the energy redistribution during loading as discussed above. We also note significant anisotropy as reflected in an imbalance in stresses between the x- and y-directions. This imbalance stems from randomness-induced anisotropy in the original networks. Overall, undulated fiber networks show slightly lower stress, with a 14% decrease in σ_x and a 18% decrease in σ_y relative to the straight networks. This discrepancy is likely a result of the undulation induced softening of the curved fibers in axial direction. More details are in the Appendix and the Discussion.

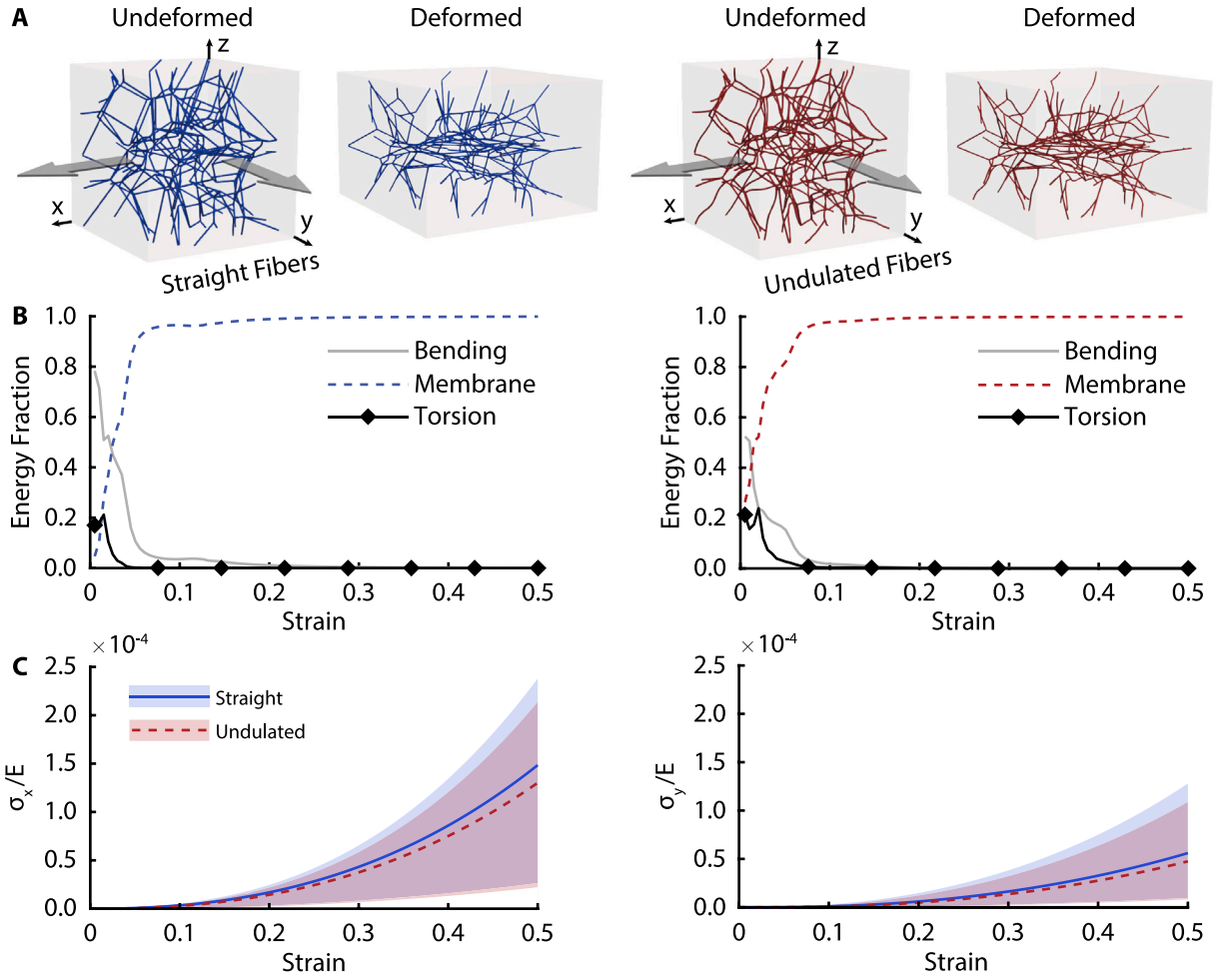

Fig. 9. Planar biaxial extension of 3D semi-flexible biopolymer networks. (A) Undeformed and deformed network comprised of straight (left) and undulated (right) fibers. (B) Energy fractions of straight (left) and undulated (right) networks (mean across three networks). (C) Stress–strain response of the straight and undulated network (mean and range across three networks). Note that the nominal stress, σ, has been normalized by the fibers' Young's modulus, E. We calculated this nominal stress as $\sigma = F/A$, where A is the area of one of the faces of the unit cube.

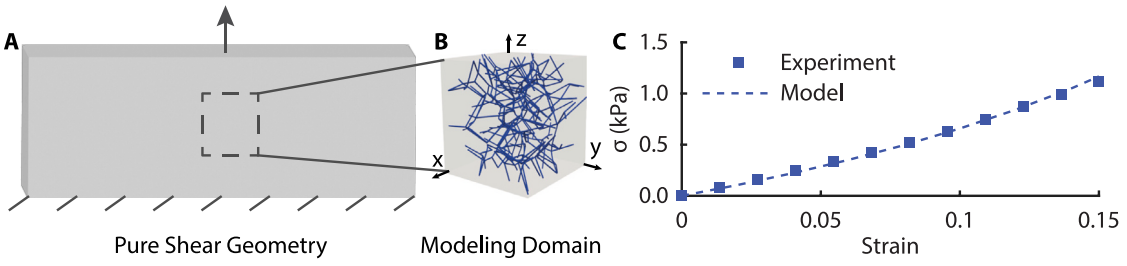

Fig. 10. Comparison of our modeling framework against fibrin experiments. (A) The reference configuration of the pure shear geometry we used in the fibrin gel experiments. (B) A unit cube network with idealized pure shear boundary conditions. (C) The model's nominal stress σ closely matches that of the experimental data, with a normalized mean square error of 0.998.

In our second virtual experiment, we simulated the deformation of a unit cube network with idealized pure shear boundary conditions, see Fig. 10. This network was fixed at the bottom $z = 0$ face, had rollers on the lateral $y = 0$ and $y = 1$ faces to restrict contraction, was left free at the $x = 0$ and $x = 1$ faces, and, finally, had a displacement applied to its top $z = 1$ face. For this experiment, we created a network that matched the volume ratio of the fibrin gels, 0.75%, and had a fibrin-representative connectivity of $z = 3.4$. We displaced the network until it reached 15% strain and then compared the resulting stress–strain data to

experimental data. We manually identified a Young's modulus that minimized the error between our experimental and simulation results, $E = 351$ MPa. The resulting normalized mean square error between the model data and the experimental data was 0.998.

4. Discussion

In this work, we introduced a novel modeling framework to simulate the mechanics of 3D semi-flexible biopolymer networks. Our framework combines large deformations, a kinematically accurate beam formulation, and a random network generation approach. Most importantly, it provides a geometrically exact solution strategy using isogeometric analysis. Therein, our work in semi-flexible biopolymer network modeling is unique.

We validated our framework and its implementation through multiple benchmark problems. Moreover, we demonstrated its use on both single-fiber and full 3D network examples, showcasing its ability to capture how fiber geometry (straight or undulated fibers) impacts fiber-level deformation modes and the macroscopic mechanics of semi-flexible biopolymer networks. Through our planar biaxial extension simulations, we recapitulated known micro-mechanical phenomena such as fiber realignment during loading (Bircher et al., 2019). Furthermore, we captured the associated transition from bending and torsion-dominated to membrane-dominated deformation modes. We also noted small but significant differences between straight and undulated fiber networks. To contextualize these observations, we recall the definition of the bending length as the square root of the ratio between bending stiffness and axial stiffness (Picu, 2011). We propose that fiber undulations modify this characteristic length; see the appendix for our derivation of the "effective" bending length. When using concrete values from our biaxial example, we find that the mean fiber length exceeds the bending length by three orders of magnitude. In other words, the initial network response is highly bending-dominated. We also find that the effective bending length is approximately forty times larger than the (unmodified) bending length; thus, explaining the apparent softening of the undulated network relative to the straight network (Islam and Picu, 2018; Ban et al., 2016).

In our planar biaxial simulations, we also tested three different randomly created networks and compared their behavior. Interestingly, while the qualitative features of energy redistributions and non-linearity in stress and strain were preserved, the stress magnitudes differed significantly. These findings highlight the well-preservedness of the qualitative features of the networks, and the sensitivity of the quantitative features. Our findings also align with experimental observations of fibrin and collagen networks, suggesting that isogeometric analysis is a promising tool to investigate real biopolymer structures (Ramanujam et al., 2024; Licup et al., 2015). This assertion was further supported by our comparison between pure shear simulations and original experiments on a fibrin gel. After fitting Young's modulus to our data, we achieve an excellent fit between both stress–strain curves.

Unlike previous approaches that employ classical finite element methods (Dey et al., 2024) or elastic discrete rods (Bergou et al., 2008) and particle methods (Crassous, 2023), our framework leverages isogeometric analysis, which offers higher accuracy per degree of freedom and exact representation of the initially curved fibers. This allows for better modeling of undulated fiber networks, capturing effects that previous studies have overlooked. An additional advantage of our isogeometric approach is its potential computational efficiency, which arises from the reduced number of primary fields compared to C^0-approaches, such as the traditional finite element method, discrete rods, or particles. In addition, because NURBS-based discretization allows for higher continuity, fewer elements are required for the same accuracy, reducing computational cost (Hughes et al., 2005). The higher continuity unique to the latter approach facilitates an *only* displacement-based formulation, where displacements are the only degrees of freedom. This leads to symmetric positive definite systems that are numerically stable and efficiently solvable. In contrast, including rotational degrees of freedom commonly adopted in discrete approaches requires mixed formulations, which result in indefinite systems that are more prone to numerical instabilities and require more complex solvers. In addition, due to the smoother curve representations inherent in NURBS-based discretization, the isogeometric approach is well suited to efficiently model contact interactions between fibers (Choi et al., 2022). This offers greater flexibility for future code extensions in this direction.

Our work is not free of limitations. For example, we did not include any degrees of freedom within the bonds between fibers. More recent work by Bauer et al. (2020) expanded their framework to include this, and others may want to expand our code similarly. Moreover, we have only used a simple constitutive law to represent the mechanical behavior at the fiber level and have not considered active stresses or fiber damage (Ronceray et al., 2016). Fortunately, our framework is not inherently limited to one material model, and others may want to expand our material choice. Finally, our fibers are not embedded in an isotropic matrix material as they are most commonly found within native soft tissues (Van Doorn et al., 2017; Dey et al., 2024; Kakaletsis et al., 2023), and we only consider a single fiber family without contact between fibers (Nedrelow et al., 2018). Along those same lines, we did not consider fiber bundles or fiber heterogeneity, all of which can be modeled with our framework as needed. However, these additions are fundamentally compatible with our framework and will thus be implemented as necessary in the future to answer specific research questions.

We believe that this approach improves geometric fidelity and provides new insights into how fiber-level mechanics contribute to macroscopic tissue behavior. Given the versatility of this framework, future work will explore its applications in experimental settings by incorporating imaging-based reconstructions of real biopolymer networks, such as those derived from confocal microscopy. This will allow us to further refine and validate the model against biological data, providing a deeper insight into the structure-function relationships of soft tissues.

5. Conclusions

In this work, we introduced, validated, and demonstrated a novel modeling framework for 3D semi-flexible biopolymer networks using isogeometric analysis. This numerical framework can accurately capture the complex geometry and mechanics of these semi-flexible biopolymer networks. Future work with this framework will provide fundamental insight into the structure-function relationship of this important class of materials. Importantly, all the code and information necessary to reproduce our work is openly available through a GitHub repository listed under "Code Availability" below.

CRediT authorship contribution statement

Matthew J. Lohr: Software, Writing – original draft, Writing – review & editing, Visualization. **Soham Mane:** Software, Conceptualization, Visualization, Investigation, Methodology, Validation, Formal analysis. **Sotirios Kakaletsis:** Data curation, Conceptualization, Software. **Grace N. Bechtel:** Investigation. **Jan N. Fuhg:** Writing – original draft, Conceptualization, Supervision, Writing – review & editing. **Berkin Dortdivanlioglu:** Writing – review & editing, Funding acquisition, Writing – original draft. **Rui Huang:** Writing – review & editing, Supervision, Writing – original draft, Funding acquisition. **Manuel K. Rausch:** Visualization, Resources, Funding acquisition, Writing – review & editing, Supervision, Methodology, Data curation, Validation, Project administration, Formal analysis, Writing – original draft, Software, Investigation, Conceptualization.

Code availability

All code required to generate, discretize, simulate, and analyze the semi-flexible biopolymer networks presented in this work are available in the GitHub repository associated with this article.

URL: https://github.com/SoftTissueBiomechanicsLab/isofin

Declaration of competing interest

The authors declare the following financial interests/personal relationships which may be considered as potential competing interests: Dr. Rausch reports financial support was provided by National Science Foundation. Dr. Dortdivanlioglu reports financial support was provided by National Science Foundation. Dr. Rausch reports a relationship with Edwards Lifesciences Corporation that includes: consulting or advisory and speaking and lecture fees. If there are other authors, they declare that they have no known competing financial interests or personal relationships that could have appeared to influence the work reported in this paper.

Acknowledgments

This work was supported by National Science Foundation grants #2046148, #2105175, #2127925, #2235856, #2438943 to Dr. Rausch, and National Science Foundation grants #2443175 and #2119716 to Dr. Dortdivanlioglu.

Appendix. Derivation of the effective bending length of undulated fiber (networks)

The classical bending length scale (Picu, 2011; Ban et al., 2016) is defined as

$$\ell_b = \sqrt{\frac{EI}{EA}}, \tag{8}$$

where EI is the bending stiffness and EA is the axial stiffness of a straight beam. This characteristic length determines whether the deformation of a beam is bending dominated ($\ell_b \ll \ell$) or stretching dominated ($\ell_b \gg \ell$), where ℓ is the average beam length.

For initially curved Euler–Bernoulli beams, the presence of geometric undulations modifies the effective axial response. This leads to an effective bending length scale given by

$$\ell^* = \sqrt{\frac{EI}{E_{\text{eff}}A}}, \tag{9}$$

where E_{eff} is the effective Young's modulus accounting for the additional compliance introduced by the initial curvature.

To compute the effective modulus, we used an energy-based approach (Timoshenko and Gere, 2012), in which we equated the external and internal virtual work and integrated over the nonuniform bending stiffness as a function of the initial sinusoidal undulations of amplitude C. Note that we assumed small undulations, i.e., $C \ll \ell$ in this derivation.

This yields

$$E_{\text{eff}} = \left(\frac{1}{E} + \frac{C^2 A}{2EI}\right)^{-1}, \tag{10}$$

where E is the Young's modulus of the material and A is the cross-sectional area.

Data availability

We made our code openly available and have included a statement to this effect in the manuscript.

References

Amuasi, H.E., Michels, M., Storm, C., 2012. Eindhoven: Technische Universiteit Eindhoven. ((Co-) promot.: Dr. MAJ Michels & Dr. C. Storm).
Arzash, S., Shivers, J.L., MacKintosh, F.C., 2020. Soft Matter 16 (29), 6784–6793.
Ban, E., Barocas, V.H., Shephard, M.S., Picu, C.R., 2016. J. Appl. Mech. (ISSN: 0021-8936) 83 (4), 041008. http://dx.doi.org/10.1115/1.4032465, ISSN: 1528-9036. URL https://asmedigitalcollection.asme.org/appliedmechanics/article/doi/10.1115/1.4032465/422257/Effect-of-Fiber-Crimp-on-the-Elasticity-of-Random.
Bastas, C., Savard, L., Jacobson, K., Connell, K., Calve, S., Ferguson, V., Luetkemeyer, C., 2025. J. Mech. Behav. Biomed. Mater. 163, 106874.
Bauer, A., Breitenberger, M., Philipp, B., Wüchner, R., Bletzinger, K.-U., 2016. Comput. Methods Appl. Mech. Engrg. 303, 101–127.
Bauer, A., Wüchner, R., Bletzinger, K.-U., 2020. Comput. Methods Appl. Mech. Engrg. 361, 112747.
Bechtel, G.N., Sugerman, G.P., Eades, T., Malinowska, Z., Bush, A.M., Saber, H., Parekh, S.H., Rausch, M.K., 2025a. Adv. Heal. Mater. (ISSN: 2192-2640) 14 (9), 2403389. http://dx.doi.org/10.1002/adhm.202403389, ISSN: 2192-2659. URL https://advanced.onlinelibrary.wiley.com/doi/10.1002/adhm.202403389.
Bechtel, G.N., Sugerman, G.P., Eades, T., Parast, L., Saber, H., Chang, A., Bush, A.M., Rausch, M.K., 2025b. Biomech. Model. Mechanobiol. (ISSN: 1617-7959) http://dx.doi.org/10.1007/s10237-025-01954-7, ISSN: 1617-7940. URL https://link.springer.com/10.1007/s10237-025-01954-7.
Bergou, M., Wardetzky, M., Robinson, S., Audoly, B., Grinspun, E., 2008. ACM Trans. Graph. (ISSN: 0730-0301) 27 (3), 1–12. http://dx.doi.org/10.1145/1360612.1360662, ISSN: 1557-7368. URL https://dl.acm.org/doi/10.1145/1360612.1360662.
Bircher, K., Zündel, M., Pensalfini, M., Ehret, A., Mazza, E., 2019. Nat. Commun. 10, 792.
Broedersz, C.P., MacKintosh, F.C., 2014. Rev. Modern Phys. 86 (3), 995.
Carleton, J., D'Amore, A., Feaver, K., Rodin, G., Sacks, M., 2015. Acta Biomater. 12, 93–101.
Chacko, Z., Hu, J., Soboyejo, W., 2023. Comprehensive Structural Integrity, second ed. 9, pp. 181–196.
Chawla, D., Thao, A., Eriten, M., Henax, C., 2024. J. Mech. Behav. Biomed. Mater. 160, 106753.
Choi, M.-J., Klinkel, S., Sauer, R.A., 2022. Comput. Mech. (ISSN: 0178-7675) 70 (6), 1107–1144. http://dx.doi.org/10.1007/s00466-022-02223-5, ISSN: 1432-0924. URL https://link.springer.com/10.1007/s00466-022-02223-5.
Cox, M.G., 1971. Comput. J. 14 (3), 272–275.
Crassous, J., 2023. Phys. Rev. E 107, 025003. http://dx.doi.org/10.1103/PhysRevE.107.025003.
De Boor, C., 1972. J. Approx. Theory 6 (1), 50–62.
Dey, M., Merson, J., Picu, R., 2024. J. Mech. Behav. Biomed. Mater. 155, 106583.
Eichinger, J., Grill, M., Kermani, I., Aydin, R., Wall, W., Humphrey, J., Cyron, C., 2021. Biomech. Model. Mechanobiol. 20, 1851–1870.
Ferruzzi, J., Bersi, M., Humphrey, J., 2013. Ann. Biomed. Eng. 41 (7), 1311–1330.
Garyfallogiannis, K., Ramanujam, R., Litvinov, R., Yu, T., Chandrasekaran, N., Bassani, J., Weisel, J., Purohit, P., Tutwiler, V., 2023. Acta Biomater. 159, 49–62.
Haese, C., Dubey, V., Mathur, M., Pouch, A., Timek, T., Rausch, M., 2025. J. Mech. Behav. Biomed. Mater. 163, 106879.
Hall, M.S., Alisafaei, F., Ban, E., Feng, X., Hui, C.-Y., Shenoy, V.B., Wu, M., 2016. Proc. Natl. Acad. Sci. 113 (49), 14043–14048.
Hashimoto, N., Kiyono, T., Saitow, F., Asada, M., Yoshida, M., 2017. PLoS One 12 (10), e0186584.
Hughes, T.J., Cottrell, J.A., Bazilevs, Y., 2005. Comput. Methods Appl. Mech. Engrg. 194 (39–41), 4135–4195.
Islam, M., Picu, R., 2018. J. Appl. Mech. 85 (8).
Jansen, K.A., Licup, A.J., Sharma, A., Rens, R., MacKintosh, F.C., Koenderink, G.H., 2018. Biophys. J. 114 (11), 2665–2678.
Kakaletsis, S., Lejeune, E., Rausch, M.K., 2023. J. Mech. Phys. Solids (ISSN: 0022-5096) 181, 105456.
Kakaletsis, S., Meador, W.D., Mathur, M., Sugerman, G.P., Jazwiec, T., Malinowski, M., Lejeune, E., Timek, T.A., Rausch, M.K., 2021. Acta Biomater. 123, 154–166.
Kallel, H., Joulain, K., 2022. Mater. Des. 220, 110800.
Kiendl, J., Bazilevs, Y., Hsu, M.-C., Wüchner, R., Bletzinger, K.-U., 2010. Comput. Methods Appl. Mech. Engrg. 199 (37–40), 2403–2416.
Korcari, A., Pryzbelski, S., Gingery, A., Loiselle, A., 2023. Connect. Tissue Res. 64 (1), 1–13.
Leng, V., Calve, S., Tepole, A.B., 2021. Comput. Methods Appl. Mech. Engrg. 387, 114160.
Licup, A., Münster, S., Sharma, A., Sheinman, M., Jawerth, L., Fabry, B., Weitz, D., MacKintosh, F., 2015. Proc. Nat. Acad. Sci. 112 (31), 9573–9578.
Ling, Y.T.T., Shi, R., Midgett, D.E., Jefferys, J.L., Quigley, H.A., Nguyen, T.D., 2019. Investig. Ophthalmol. Vis. Sci. 60 (7), 2406–2422.
Lo, S., 1992. Comput. Struct. 44 (1–2), 147–157.
Lohr, M., Bechtel, G., Dortdivanlioglu, B., Rausch, M., 2025. Int. J. Fract. 249, 9.
Lohr, M., Sugerman, G., Kakaletsis, S., Lejeune, E., Rausch, M., 2022. Phil. Trans. R. Soc. A 380.
Marino, E., 2017. Comput. Methods Appl. Mech. Engrg. 324, 546–572.
Matange, K., Marland, E., Frenkel-Pinter, M., Williams, L., 2025. Acc. Chem. Res. 58, 659–672.
Mathur, M., Meador, W.D., Malinowski, M., Jazwiec, T., Timek, T.A., Rausch, M.K., 2022. Eng. Comput. 38 (5), 3835–3848.
Meador, W., Mathur, M., Kakaletsis, S., Lin, C., Bersi, M., Rausch, M., 2022. Extrem. Mech. Lett. 55, 101799.
Meador, W.D., Mathur, M., Sugerman, G.P., Malinowski, M., Jazwiec, T., Wang, X., Lacerda, C.M., Timek, T.A., Rausch, M.K., 2020a. Elife 9, e63855.
Meador, W.D., Sugerman, G.P., Story, H.M., Seifert, A.W., Bersi, M.R., Tepole, A.B., Rausch, M.K., 2020b. Acta Biomater. 101, 403–413.
Merson, J., Picu, R., 2020. Int. J. Solids Struct. 206, 314–321.
Middendorf, J., Ita, M., Winkelstein, B., Barocas, V., 2021. Biomech. Model. Mechanobiol. 20, 2269–2285.
Nedrelow, D.S., Bankwala, D., Hyypio, J.D., Lai, V.K., Barocas, V.H., 2018. Acta Biomater. 72, 306–315.
Negi, V., Picu, R., 2019. J. Mech. Phys. Solids 122, 418–434.
Pearce, D., Nemcek, M., Witzenburg, C., 2023. Biophys. Rev. 15, 329–353.
Picu, R., 2011. Soft Matter 7 (15), 6768–6785.
Picu, C., Ganghoffer, J.-F., Guazzelli, E., Rammerstorfer, F., Wall, W., Schrefler, B., Serafini, P., 2020. Mechanics of Fibrous Materials and Applications. Springer.
Piegl, L., Tiller, W., 1996. The NURBS book. Springer Science & Business Media.
Raknes, S., Deng, X., Bazilevs, Y., Benson, D., Mathisen, K., Kvamsdal, T., 2013. Comput. Methods Appl. Mech. Engrg. 263, 127–143.
Ramanujam, R., Garyfallogiannis, K., Litvinov, R., Bassani, J., Weisel, J., Purohit, P., Tutwiler, V., 2024. R. Soc. Chem. 20, 4184–4196.
Riedel, L., Wö"ssner, V., Kempf, D., Ziebert, F., Bastian, P., Schwarz, U., 2025. J. Mech. Phys. Solids 195, 105950.
Rodney, D., Fivel, M., Dendievel, R., 2005. Phys. Rev. Lett. 95 (10), 108004.
Ronceray, P., Broedersz, C.P., Lenz, M., 2016. Proc. Natl. Acad. Sci. 113 (11), 2827–2832.
Runnels, C.M., Lanier, K.A., Williams, J.K., Bowman, J.C., Petrov, A.S., Hud, N.V., Williams, L.D., 2018. J. Mol. Evol. 86 (9), 598–610.
Shkarin, R., Shkarin, A., Shkarina, S., Cecilia, A., Surmenev, R.A., Surmeneva, M.A., Weinhardt, V., Baumbach, T., Mikut, R., 2019. PLoS One 14 (4), e0215137.
Stylianopoulos, T., Barocas, V.H., 2007. Comput. Methods Appl. Mech. Engrg. 196 (31–32), 2981–2990.

Sugerman, G.P., Bechtel, G.N., Malinowska, Z., Parekh, S.H., Rausch, M.K., 2024. J. Mech. Behav. Biomed. Mater. (ISSN: 17516161) 154, 106508. http://dx.doi.org/10.1016/j.jmbbm.2024.106508, URL https://linkinghub.elsevier.com/retrieve/pii/S1751616124001401.
Sugerman, G.P., Chokshi, A., Rausch, M.K., 2021. Curr. Protoc. (ISSN: 2691-1299) 1 (7), e197. http://dx.doi.org/10.1002/cpz1.197, ISSN: 2691-1299. URL https://currentprotocols.onlinelibrary.wiley.com/doi/10.1002/cpz1.197.
Tang, V., 2020. Mol. Biol. Cell 31.
Tarakanova, A., Yeo, G.C., Baldock, C., Weiss, A.S., Buehler, M.J., 2018. Proc. Natl. Acad. Sci. 115 (28), 7338–7343.
Tepole, A.B., Kabaria, H., Bletzinger, K.-U., Kuhl, E., 2015. Comput. Methods Appl. Mech. Engrg. 293, 328–347.
Timoshenko, S., 1953. History of strength of materials McGraw-Hill book company. Inc, New York/Toronto/London.
Timoshenko, S.P., Gere, J.M., 2012. second ed. Dover Civil and Mechanical Engineering, Dover Publications, Newburyport, ISBN: 978-0-486-13480-2.
Tsingos, E., Bakker, B., Keijzer, K., Hupkes, H., 2023. Biophys. J. 122, 2609–2622.
Van Doorn, J.M., Lageschaar, L., Sprakel, J., van der Gucht, J., 2017. Phys. Rev. E 95 (4), 042503.
Wang, Y., Kumar, S., Nisar, A., Bonn, M., Rausch, M.K., Parekh, S.H., 2021. Acta Biomater. 121, 383–392.
Yadav, P., Yadav, H., Shah, V.G., Shah, G., Dhaka, G., 2015. J. Clin. Diagn. Res.: JCDR 9 (9), ZE21.
Zakharov, A., Awan, M., Gopinath, A., Lee, S., Ramasubramanian, A., Dasbiswas, K., 2024. Sci. Adv. 10 (2), eadh1265.